Noninductive plasma initiation and startup in the DIII-D tokamak

2011 Nucl. Fusion 51 083015

(http://iopscience.iop.org/0029-5515/51/8/083015)

IOP Publishing and International Atomic Energy Agency Nuclear Fusion
Nucl. Fusion **51** (2011) 083015 (9pp) doi:10.1088/0029-5515/51/8/083015

Noninductive plasma initiation and startup in the DIII-D tokamak

G.L. Jackson[1], D.A. Humphreys[1], A.W. Hyatt[1], J.M. Lohr[1], T.C. Luce[1] and J.H. Yu[2]

[1] General Atomics, PO Box 85608, San Diego, CA 92186-5608, USA
[2] University of California, 9500 Gilman Dr., La Jolla, San Diego, CA 92093-0417, USA

Received 4 February 2011, accepted for publication 8 June 2011
Published 12 July 2011
Online at stacks.iop.org/NF/51/083015

Abstract
Noninductive plasma startup with second harmonic electron cyclotron heating has been studied in DIII-D. Plasma currents up to 33 kA have been obtained in this phase. The maximum current obtained was primarily limited by the experimental time and does not necessarily represent the highest achievable current. The dominant physical mechanism for the observed current is the Pfirsch–Schlüter current on open field lines. Closed flux surfaces have been observed, but in a rather limited region, compared with previous experiments in spherical tokamaks. This method of plasma initiation and initial current ramp might be used in future burning plasma devices in conjunction with other current drive techniques to provide a fully noninductive startup.

(Some figures in this article are in colour only in the electronic version)

1. Introduction

Initiation and startup of plasma discharges without a central solenoid (CS) (or a much reduced one) provides distinct advantages for burning plasma devices. With a CS smaller than that required to supply the entire flux to reach the operating current, the engineering design and cost are simplified and the tokamak can be made more compact. Although the engineering problem may be easier, noninductive startup introduces a new set of complexities. A fully noninductive plasma current ramp-up to flattop will probably require the combination of several techniques. Plasma initiation and the initial current formation might best be done using electron cyclotron (EC) waves. In this paper we report on plasma breakdown and toroidal plasma current initiation using EC heating.

Several tokamaks have explored EC plasma current startup. Low aspect ratio tokamaks such as spherical tokamaks (STs) have been especially successful [1–4], since the pressure-driven bootstrap current scales as $\varepsilon^{1/2}$, where ε is the inverse aspect ratio, a/R. Higher aspect ratio tokamaks have also observed noninductively driven EC currents during startup, e.g. T-IIU [5], WT-3 [6], DIII-D [7], JT-60U [8] and KSTAR [9]. In the experiments reported here, up to 33 kA has been driven with 2 MW of second harmonic EC power (X-mode). We note that the MAST ST has achieved similar values of I_p with fundamental EC heating and mode conversion to electron Bernstein waves (EBWs) [4]. Maximum reported currents in other devices were 20 kA or less.

The work reported here is an extension of DIII-D experiments to benchmark scenarios for successful startup of the ITER tokamak [10]. In these scenarios using EC pre-ionization, noninductive plasma currents were sometimes observed. This led to experiments, reported here, to explore conditions to increase the plasma current and to characterize these discharges.

The DIII-D tokamak, with a non-circular cross-section, controls plasma shape using 18 field-shaping coils [11], although only four of these coils were energized to provide vertical field in these experiments (figure 1). The focus of this paper is on EC driven noninductive toroidal plasma current and we refer to the current in this phase as I_{pre}. Later in time, there is a transition to the normal ohmically heated plasma when inductive toroidal loop voltage, V_{loop}, is applied by a separate coil system. One turn loop voltage produced by this system is defined as $V_{loop} = -d\psi/dt$, where ψ is calculated from a subset of the flux loops shown in figure 1. The transition from noninductive currents, I_{pre}, to inductively driven plasmas will be discussed later.

A cross-section of the DIII-D tokamak with some of the diagnostics used in this work is shown in figure 1. Both flux loops and poloidal magnetic field probes are used to calculate poloidal flux and plasma currents inside the vacuum vessel, as discussed in section 3. The ECE radiometer infers electron temperature profiles when the plasma is optically dense [12]. If the plasma is not optically dense, the radiometer gives a 'radiation temperature' that can be more (or less) than the average energy of the electrons, depending on the details of the distribution function. Microwave interferometers measure

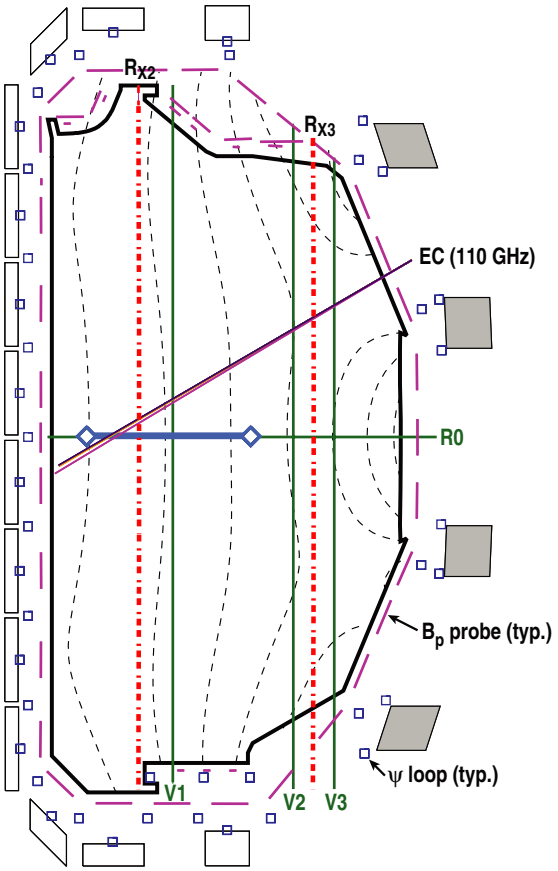

Figure 1. Cross-section of the DIII-D tokamak and main diagnostics for I_{pre} experiments. Eighteen poloidal field coils are shown as boxes and the four active outer coils enabled during this experiment are shaded. Vacuum flux surfaces are shown as dashed lines and R_{X2} and R_{X3} EC resonant radii are indicated as dashed–dotted lines. The radial extent of the 40 channel ECE radiometer is delineated by diamonds. Interferometer paths, V1, V2, V3, and R0 are also shown. Flux loops are indicated as small squares and the location of poloidal magnetic probes are shown as short straight lines, both outside the outline of the DIII-D plasma facing surface. Note that ECE locations and EC resonant radii shift radially as B_T changes. A typical example, $B_T = 1.56$ T (#140857) is shown.

electron density. In these plasmas, a large fraction of the plasma current can occur on open field lines [2, 3, 7] filling the entire vacuum vessel and hence we define the average electron density as

$$\overline{n}_{eNN} = \int^{L} n_e \, dl / L_{NN}, \quad (1)$$

where L_{NN} is the total interferometer path length inside the vacuum vessel and NN refers to the density chord (R0, V1, V2 or V3) shown in figure 1. For the highest values of I_{pre} the electron temperature and density are sufficient for Thomson scattering (TS) to measure T_e and $\bar{n}_e$ profiles. For all discharges in this paper, deuterium was used as the fill gas.

The DIII-D EC system consists of six 110 GHz gyrotrons each with a nominal output power of 1 MW at the tube. The gyrotron power is routed by circular waveguides (HE_{11}) to steerable mirrors that inject the EC power into the tokamak from the low-field side (LFS). Both X-mode and O-mode polarizations are possible with this system and both the poloidal and toroidal injection angles can be changed between discharges. For the work reported here, second harmonic X-mode (X2) EC power was injected nearly radially (2° from perpendicular to the toroidal magnetic field). A 60 GHz ECH system was previously used in DIII-D, injecting from the high-field side (HFS), and noninductive startup with this system [7] will be compared with the present results in section 4.

2. Experimental results

As discussed in section 1, EC pre-ionization has produced both breakdown and noninductive toroidal plasma currents. An example of such a noninductive toroidal plasma current, I_{pre}, is shown in figure 2. In this discharge, 2.2 MW of second harmonic X-mode ECH is applied starting at $t = -40$ ms and breakdown, measured by D_α emission, initiates promptly (within 1 ms) (figure 2(*e*)). A small current ($I_{pre} \approx 5$ kA) is initially observed ($t \leqslant -34$ ms) followed by a spontaneous transition with I_{pre} increasing to 24 kA before the CS ramp starts at -8 ms, figure 2(*a*). The spontaneous transition is similar to observations reported in [3]. Loop voltage (figure 2(*c*)) is negative or zero during this phase (the CS induces a positive V_{loop}, $t > -8$ ms). Since the current in the CS and all PF coils are constant in this phase (-40 to -8 ms), the plasma current is fully driven noninductively. The increase in C^{III} intensity, figure 2(*e*), is delayed compared with D_α, indicating the evolution in plasma temperature, although burnthrough of C^{III} is not achieved until after the end of the noninductive phase, presumably due to ohmic heating (OH). The temporal evolution of electron temperature, T_{ECE}, measured by the ECE radiometer at two radial locations is plotted in figure 2(*f*). We note that the overshoot in T_{ECE} $-$ 39 $\leqslant t \leqslant -34$ ms may be due to the plasma not being optically dense. Neutral pressure measured by a fast ionization gauge initially overshoots (figure 2(*d*)), although it has not been established whether this effect is instrumental or caused by local changes of neutral pressure at the gauge. The neutral pressure then decreases exponentially throughout the noninductive phase with a time constant of 16 ms (the time constant of pressure gauge is ≈2–3 ms). Except for early times, $t \leqslant -32$ ms, the average electron density (figure 2(*b*)) is nearly the same whether measured vertically or horizontally (figure 1), except for the vertical chord (V1) near the EC resonance, indicating that the electron density is rather uniform over most of the vessel volume.

A fast visible camera [13] viewing D_α light indicates that breakdown occurs near the second harmonic EC resonant radius, R_{X2} (figure 3(*b*)). The plasma rapidly expands [10] and during most of the noninductive phase it is limited on the LFS, above and below the outer midplane (figure 3(*c*)). After the CS ramp begins, the plasma fills the vessel and radial position control is applied ($t \geqslant +5$ ms). For $t \geqslant 10$ ms, the plasma is well limited on the HFS (figure 3(*e*)).

A limited set of parameter scans were carried out, shown in figure 4. The strongest increase in I_{pre} was observed when increasing the neutral pressure (figure 4(*a*)) or decreasing the toroidal field (hence moving R_{X2} towards the HFS). Little effect was observed by changing the applied vertical field, B_z, although the range of this scan was limited. Also, only modest effects were observed by increasing EC power

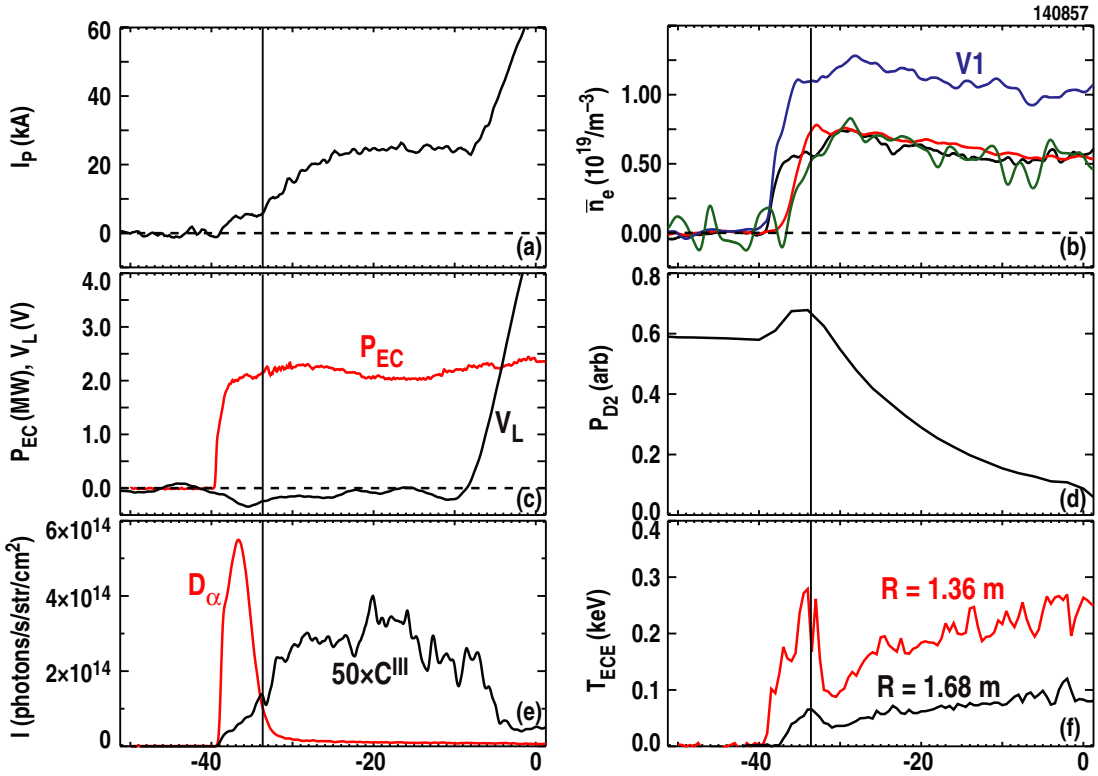

Figure 2. (*a*) I_p with a plateau, $I_{pre} = 5$ kA, $t \leqslant -33.7$ ms (vertical line) followed by a spontaneous transition. (*b*) Density from interferometers, using equation (1). $V1$ ($R_{V1} = 1.48$ m) is nearest the EC resonance ($R_{X2} = 1.34$ m) and indicates highest density while other chords (R0, V2, and V3) show similar densities. Locations of interferometer chords are shown in figure 1. Also plotted are (*c*) EC power and one-turn loop voltage, V_L (measured on the HFS, $R_0 = 0.89$ m, near the midplane), (*d*) neutral pressure measured by a fast ion gauge, (*e*) midplane D_α and C^{III} emission measured by a filterscope array, and (*f*) ECE temperature at two radial locations. $B_T = 1.56$ T, $B_z = -50$ G (constant during the noninductive phase), and $P_{prefill} = 0.36$ mTorr.

(figure 4(*d*)), although this scan was performed at low neutral pressure and high B_T, and hence was at relatively low plasma currents.

The results shown in figure 4 suggested that higher plasma current could be obtained at reduced B_T ($R_{X2} < R_0$), where $R_0 = 1.7$ m is the DIII-D major radius. Furthermore, since the plasma was limited on the LFS, a more negative B_z, producing a larger inward force, $j_\phi \times B_z$, on the plasma, could also be beneficial in achieving force balance at higher plasma current. With this prescription, the highest value of I_{pre} to date, 33 kA, has been obtained (figure 5(*a*)). At this higher current and lower prefill, the density profile was not as uniform (figure 5(*d*)) as observed at higher pressures, e.g. figure 2(*b*). At the most negative value of B_z (figure 5(*b*)), I_{pre} stops increasing, and actually begins to decrease. Although this is consistent with the observations in [7], we note that the temporal variation in B_z due to the outer PF coils in figure 5(*b*) can also produce a net change of flux inside the torus in the direction that drives positive I_p (note that the induced one-turn voltage is not constant in major radius in this case). Since plasma current is changing and also possibly the position of current centroid, the net contribution to increasing I_p by ramping B_z has not been evaluated. T_e and n_e profiles for this discharge are shown in figure 6. The TS density profile is in good agreement with n_e from the interferometers (figure 6(*b*)) and the ECE and TS temperature profiles also show good agreement.

3. Flux reconstruction and toroidal plasma current density

A key issue in this work is the distribution of poloidal flux and plasma current. We use the filament code JFIT, which can solve for an arbitrary current distribution and calculate the flux for that distribution. The JFIT reconstruction first solves for toroidal plasma current on a specified grid using measurements from arrays of magnetic field probes and flux loops shown in figure 1 and then calculates the flux from this reconstruction [14]. From this analysis, JFIT can then determine current densities of arbitrary distribution rather than fitting a prescribed current profile (e.g. EFIT) and as such it is especially useful in determining the toroidal current on open field lines. During the transition from noninductive to inductive current drive, significant toroidal currents flow in the vacuum vessel. The total vessel current is measured using a combination of a Rogowski coil outside the vacuum vessel and a poloidally complete set of magnetic field probes (figure 1) inside producing a pseudo-Rogowski. This current is then included in the fit using a 28-element vacuum vessel model and the plasma current distribution is calculated. We note that although this reconstruction is consistent with Maxwell's equations, no other constraints have been applied and hence these solutions should only be used as an approximate indication of the current density.

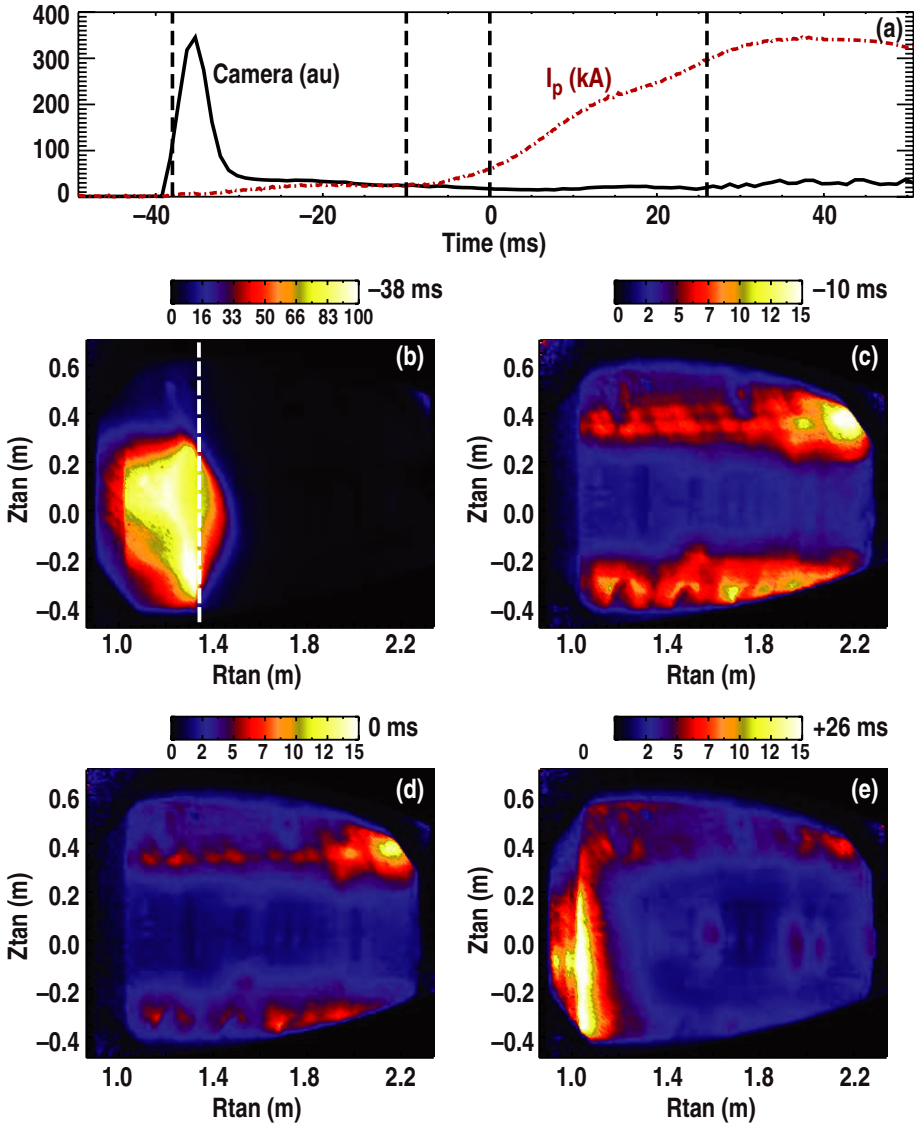

Figure 3. (*a*) Camera intensity and I_p with dashed lines indicating times of images in (*b*)–(*e*). D_α images at four times, (*b*)–(*e*) from a fast framing camera viewing tangentially. The R_{X2} resonant radius is plotted as a vertical line (*b*).

The temporal evolution of both the flux and plasma current density is shown in figures 7 and 8, respectively. Initially all current is on open field lines (figure 8(*a*)) and I_{pre} is located near X2 resonant radius on the HFS of the tokamak. This is the Pfirsch–Schlüter (PS) current discussed in [3], and plasma current remains constant, ≈5 kA, for 3.4 ms. A transition is observed at $t = -33.7$ ms (figure 2(*a*)) and plasma current begins increasing towards the LFS (figure 8(*b*)). As the current continues to increase, closed flux surfaces are observed (figure 7(*c*)), although the region inside the LCFS is rather small. During the noninductive phase (figure 8(*c*)), plasma current is highest on the LFS, above and below the midplane. Consistent with this observation, the maximum D_α intensity was also above and below the midplane on the LFS side (figure 3(*c*)), suggesting that the plasma was interacting with the wall in these regions. Inductive voltage begins increasing at $t = -8$ ms and both the region inside the LCFS and the current region broaden, figures 7(*d*) and 8(*d*). The current centroid also moves towards the HFS. By $t = 0$ ms, the plasma volume inside the LCFS is well established (figure 7(*e*)) and by $t > 10$ ms the plasma is well limited on the inside wall. At this time current density inferred from JFIT is distributed around the outer part of the plasma, typical of the early formation of inductively driven plasmas before current can sufficiently penetrate. The lack of a uniform current density around the plasma periphery as current is driven inside the LCFS, e.g. figures 8(*e*) and (*f*), shows the limitations of the present JFIT reconstruction technique. Additional physical constraints are being considered to improve this fitting technique.

4. Discussion

Noninductive current startup has been obtained reliably in the DIII-D tokamak with many characteristics similar to those observed in other high aspect ratio tokamaks and STs. Immediately after the onset of EC heating, toroidal plasma currents flow to reduce the charge separation induced by $\nabla B \times B$ and curvature drifts. This is the PS current [15].

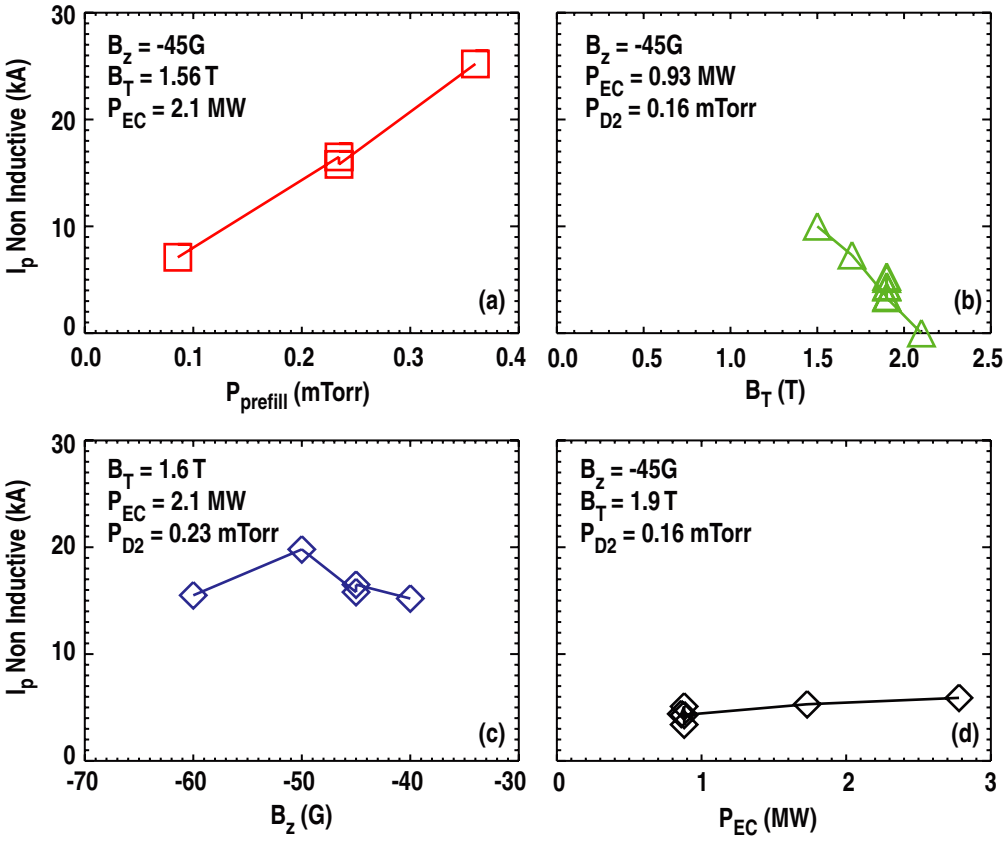

Figure 4. Noninductive plasma current as a function of (*a*) neutral prefill pressure, P_{prefill}, (*b*) toroidal field, B_{T}, (*c*) programmed vertical field, B_z, and (*d*) EC heating power, P_{EC}.

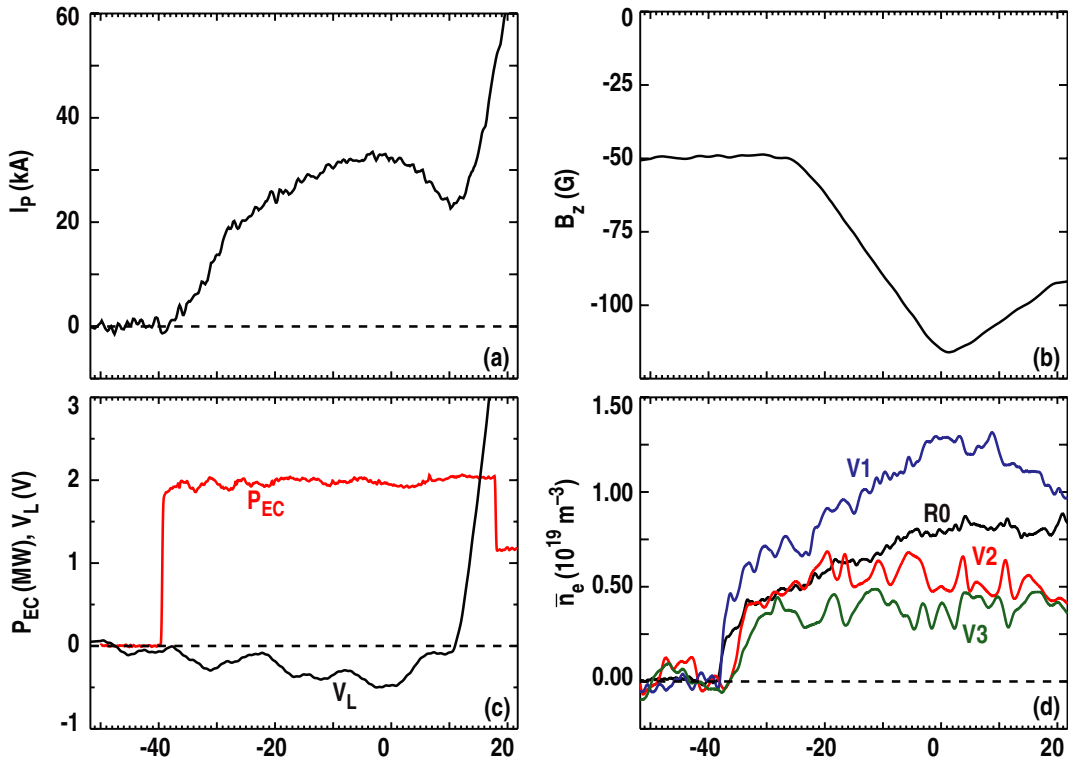

Figure 5. (*a*) Highest I_{pre} (#142100) obtained by transiently decreasing B_z, (*b*). Also shown are (*c*) one-turn loop voltage and EC power and (*d*) average plasma density (equation (1)). Locations of four interferometer chords V1, V2, V3 and R0 are shown in figure 1.

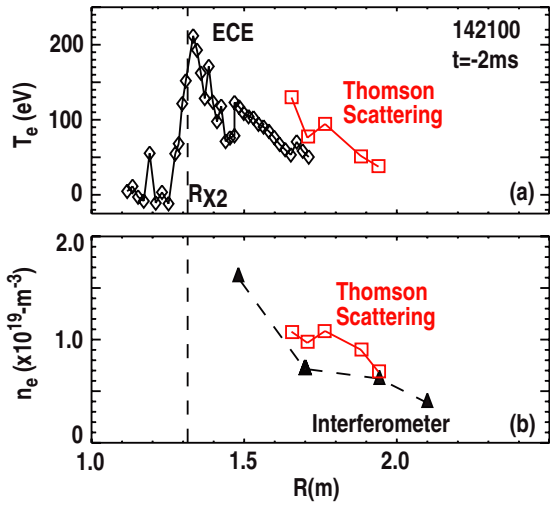

Figure 6. (*a*) T_e and (*b*) n_e profiles (squares) from TS data. Also shown are (*a*) electron temperature from ECE measurements (diamonds) and (*b*) average electron density (equation (1)) from the IR interferometer (triangles). For plotting purposes density chord R_0 is shown at the DIII-D major radius, $R_0 = 1.7$ m. R_{X2} resonance is plotted as a vertical dashed line. $B_T = 1.53$T, $R_{X2} = 1.31$ m, $B_z = -45$ G and $P_{prefill} = 0.16$ mTorr.

In normal tokamak operation with closed flux surfaces, the PS effect induces currents in such a way that there is no net current. However, on open field lines with an applied vertical field, such as the cases in this paper, PS currents can produce a net toroidal current and charge flow produces a reduction in the electric field. The remaining vertical electric field from the charge separation produces a net $\boldsymbol{E} \times \boldsymbol{B}$ force radially outwards and this allows the plasma to fill most of the vacuum vessel volume. This expansion has been previously observed with a fast framing camera in DIII-D [10].

A low current plateau is often observed followed by a rapid increase in I_{pre} as shown in figure 2. This has been attributed to formation of closed flux surfaces in ST devices, e.g. [3], although the small region inside the LCFS in DIII-D (figure 7(*c*)) may suggest a different physical mechanism in DIII-D. An alternative explanation for DIII-D may simply be that the plateau in current is related to the ionization of the neutral gas and after burnthrough of D_α (figure 2(*e*)) the plasma volume begins increasing due to $\boldsymbol{E} \times \boldsymbol{B}$ expansion thus driving larger PS currents. Previous work [10] showed the plasma expanding with a velocity of $\approx$90 m s^{-1} ($P_{EC} = 2$ MW). This would correspond to 11 ms for the initial plasma to reach the LFS limiting surfaces in figure 2 and this is approximately

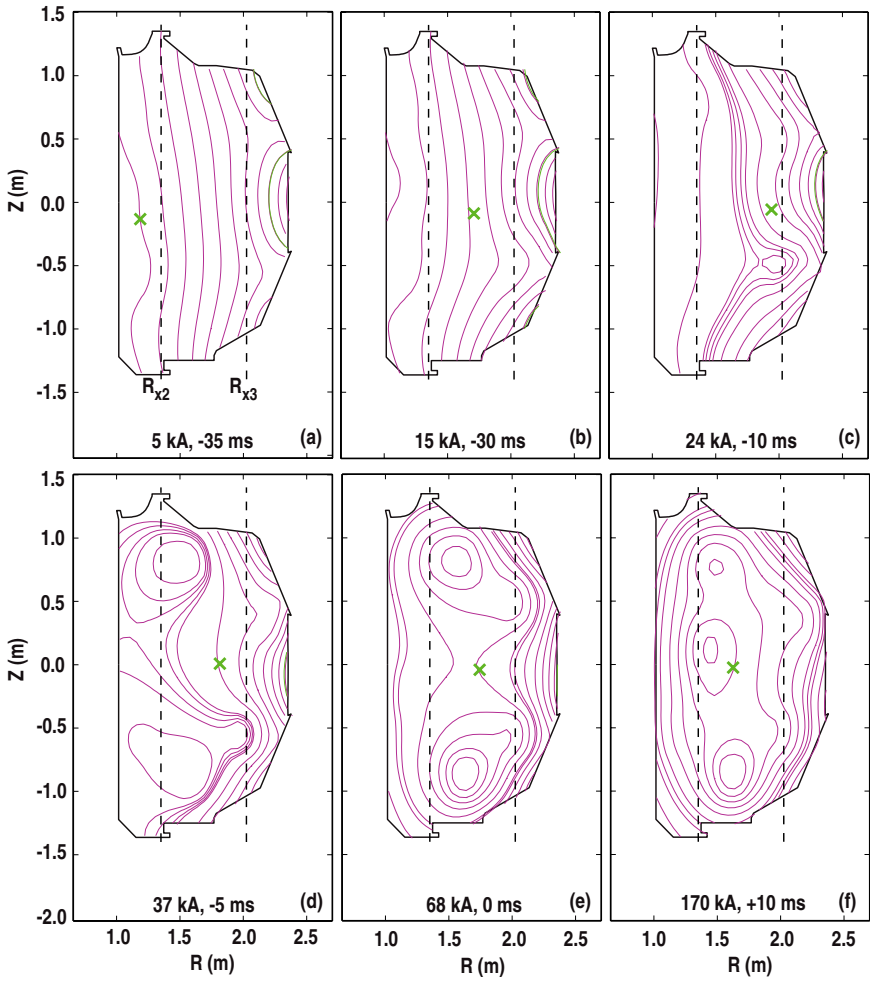

Figure 7. Startup flux plots using the JFIT code for the discharge shown in figure 3 (#140857). The first three times, (*a*)–(*c*), are in the noninductive phase and the last three, (*d*)–(*f*), illustrate the transition to the inductive phase. Crosses indicate the geometric centre of the plasma current calculated by JFIT. The inductive current ramp begins at $t = -8$ ms.

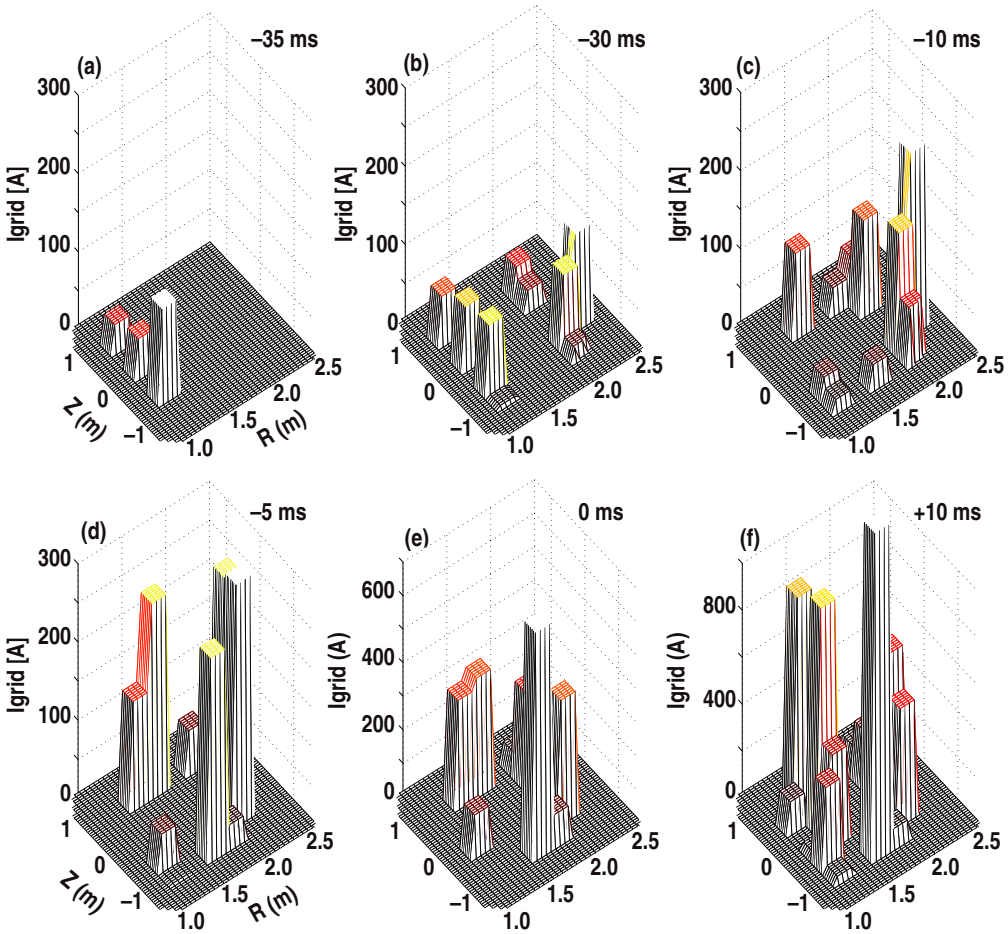

Figure 8. Current density calculated from JFIT at the same times as in figure 7 (#140857).

the time, −23 ms in figure 2, when plasma current reaches its maximum value. Further experiments are necessary to identify the mechanism for the initial current plateau and subsequent increase in plasma current.

The toroidal PS current density can be written [7]

$$j_{\mathrm{Tor}} \approx -2p_{\mathrm{e}}/(RB_z), \tag{2}$$

where p_{e} is the electron pressure.

From this we estimate an upper bound of $I_{\mathrm{PS}} = 29\,\mathrm{kA}$ at $t = -23\,\mathrm{ms}$ in discharge 140857. This assumes that the plasma fills the vessel volume for $R \geqslant R_{\mathrm{X2}}$. The estimate of I_{PS} is close to the measured value $I_{\mathrm{pre}} = 24\,\mathrm{kA}$, and we conclude that PS current is the dominant noninductive current source in these discharges. We note that banana orbits producing trapped particle current are not as likely as in ST discharges or the work reported in [1] where field curvature is much higher. This was the mechanism reported in [3] to produce the spontaneous transition leading to a bootstrap current driven plasma. In regions with closed flux surfaces, the flux surface-averaged bootstrap current can be written [15]

$$j_{\mathrm{BS}} = (-\varepsilon^{1/2}/B_{\mathrm{p}})[2.44\,\mathrm{d}p_{\mathrm{e}}/\mathrm{d}r - 1.75n_{\mathrm{e}}\,\mathrm{d}T_{\mathrm{e}}/\mathrm{d}r], \tag{3}$$

assuming $T_{\mathrm{i}} \ll T_{\mathrm{e}}$ and $\varepsilon \ll 1$.

Note that j in both equations (2) and (3) have a $-p_{\mathrm{e}}/B_{\mathrm{p}}$ dependence ($B_{\mathrm{p}} \approx B_z$ in equation (2)) making it difficult to experimentally determine which mechanism dominates. As noted in [7] other effects, namely current carried by toroidal precession of banana orbits and detrapping (leading to passing particles) also have the same dependences. However, it is clear that increasing the electron pressure is important in maximizing I_{pre}.

As noted above, the magnetic topology is very different in the present experiments compared with an ST configuration or previous DIII-D noninductive startup work. The vacuum flux for a typical discharge reported in [7] is shown in figure 9. This flux was achieved by a unique programming of the DIII-D PF coil set and was designed to provide a large fraction of trapped particles, similar to CDX-U [1]. In the present work, e.g. figure 1, vacuum flux topology is similar to that used for a conventional inductive scenario except that an additional vertical field has been found necessary to optimize breakdown and maximize I_{pre}. The small region enclosing the LCFS in figure 7(*e*) may be due to this different topology and higher aspect ratio, making the possible bootstrap current smaller than these previous experiments. We estimate that only 0.9 kA, or 3% of the total current is inside the LCFS in figure 7(*e*), further evidence the PS current is the dominant mechanism in these discharges. It is remarkable that these discharges exhibit many of the same characteristics observed in ST devices, including the spontaneous transition described in section 2. However, as noted previously, the physical mechanism for this

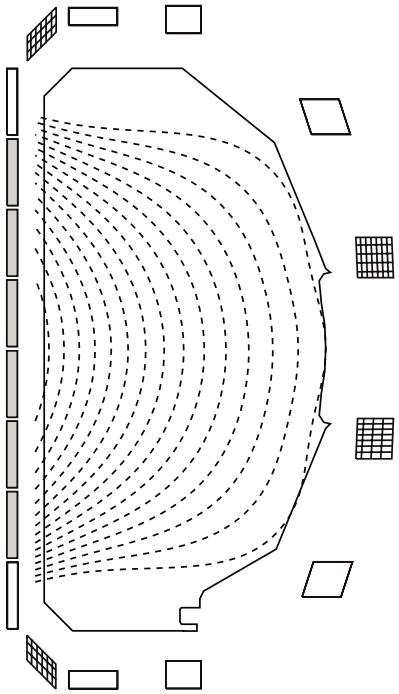

Figure 9. Vacuum flux for a previous DIII-D experiment (1993, #78769) from [7]. Poloidal field configuration was programmed to provide large flux curvature and is not the normal DIII-D startup scenario. PF coils with positive current are shaded, those with negative current are cross-hatched.

transition has not been identified and may be different than that of STs.

In order to fully analyse the possible role of bootstrap current or current drive mechanisms other than PS in this noninductive configuration, improved 2D profile diagnostics will be required. Further optimization of the parameters shown in figure 4 should also increase I_{pre} and may expand the region inside the LCFS.

Electron temperature profiles shown in figure 6 suggest that EC power deposition initially occurs near the EC X2 resonant radius. Camera images show that ionization, inferred from D_α emission, initially is observed over a large vertical range near R_{X2}, implying multipass absorption (figure 3(a)). Toray-GA modelling [16] shows that approximately 50% of the first-pass EC power is deposited in this resonant layer. Assuming an upper bound of density and temperature equal to that at the X2 location, X3 first pass absorption is calculated to be <0.4%. Although toroidal current is observed near the X2 resonant radius and dominates early in time, the region inside the LCFS occurs near the X3 resonant radius (figure 7(c)) and this is also where the largest current densities are observed. That this current density is off-midplane may be due to minima in the mod(B_{pol}) vacuum fields near these locations. The physical mechanisms that produce this current distribution have not been identified. Bootstrap driven currents could produce the localized high toroidal current densities, but a local source of heat deposition is required to produce the necessary pressure gradients. EBW heating has been observed in ST experiments at higher harmonic EC resonances [3] but the required electron densities to produce this effect are too low in DIII-D. Trapped particle electron distributions might contribute to these plasma currents, but a more detailed analysis requires additional diagnostics and experiments.

5. Conclusions

Breakdown and noninductive plasma currents up to 24 kA have been obtained in the DIII-D tokamak with EC heating alone. A B_z ramp using the outer PF coils to achieve force balance at higher plasma current has further increased this plasma current to 33 kA. The contribution of additional flux from the time varying B_z to the increase in plasma current has not yet been evaluated. We note that in this initial work, the maximum achievable current has not been determined, and further scans may produce higher NI currents. The temporal behaviour of the plasma current is similar to that observed in ST devices with an initial plateau due to current on open field lines followed by a spontaneous transition to higher currents, although the mechanism driving this higher current may not be the same in DIII-D.

Noninductive startup may be useful for ITER and future burning plasma devices. For example, the commissioning phase of ITER requires low plasma currents. As currently envisaged, EC pre-ionization alone may allow a sufficiently low *inductive* voltage to obtain well controlled low levels of plasma current. Without pre-ionization, higher voltage is required for breakdown and because of the long time constant of the vessel wall, the resulting higher plasma current can potentially damage internal vessel components that are largely unprotected during this phase. Noninductive startup might provide an alternate means of commissioning ITER systems at acceptable levels of plasma current.

Noninductive startup of burning plasma devices such as FDF [17] might also use EC for the initial phase followed by combinations of other noninductive techniques, e.g. lower hybrid CD [18], neutral beam CD [19] and ECCD [20] or methods that do not use a central solenoid such as a solenoidless inductive current ramp [21].

This work demonstrates that EC pre-ionization and subsequent toroidal plasma current can provide a noninductive startup scenario in a medium sized tokamak with aspect ratio similar to ITER ($1/\varepsilon_{\mathrm{DIII=D}} = 2.5$ and $1/\varepsilon_{\mathrm{ITER}} = 3.1$). The resulting current can complement other noninductive techniques that might provide a viable scenario for a fully noninductive plasma.

Acknowledgments

This work was supported by the US Department of Energy under DE-FC02-04ER54698 and DE-FG02-07ER54917.

References

[1] Forest C.B., Hwang Y.S., Ono M. and Darrow D.S. 1992 *Phys. Rev. Lett.* **68** 3559
[2] Ejiri A. *et al* 2006 *Nucl. Fusion* **46** 709
[3] Yoshinaga T., Uchida M., Tanaka H. and Maekawa T. 2006 *Phys. Rev. Lett.* **96** 125005
[4] Shevchenko V.F. *et al* 2010 *Nucl. Fusion.* **50** 22004
[5] Toi K. *et al* 1984 *Phys. Rev. Lett.* **52** 2144
[6] Tanaka S. *et al* 1993 *Nucl. Fusion* **33** 505
[7] Forest C.B. *et al* 1994 *Phys. Plasmas* **1** 1568

[8] Uchida M. *et al* 2011 Generation of initial closed flux surface by ECH at conventional aspect ratio of $R/a \sim 3$; experiments on the LATE device and JT-60U tokamak *Nucl. Fusion* submitted
[9] Bae Y.S. *et al* 2009 *Nucl. Fusion* **49** 022001
[10] Jackson G.L. *et al* 2010 *Phys. Plasmas* **17** 056116
[11] Luxon J.L. 2002 *Nucl. Fusion* **42** 614
[12] Austin M.E., Ellis R.F., James R.A. and Luce T.C. 1996 *Phys. Plasmas* **3** 3725
[13] Yu J. H. and Van Zeeland M.A. 2008 *Rev. Sci. Instrum.* **79** 10F516
[14] Humphreys D.A. and Kellman A.G. 1999 *Phys. Plasmas* **6** 2742
[15] Wesson J. 1997 *Tokamaks* 2nd edn (Oxford: Clarendon)
[16] Matsuda K. 1989 *IEEE Trans. Plasma Sci.* **17** 6
[17] Chan, V.S. *et al* 2011 A fusion development facility on the critical path to fusion energy *Nucl. Fusion* submitted
[18] Jobes F. *et al* 1984 *Phys. Rev. Lett.* **52** 1005
[19] Simonen T.C. *et al* 1988 *Phys. Rev. Lett.* **61** 1720
[20] Prater R. 2004 *Phys. Plasmas* **11** 2349
[21] Leuer J.A. *et al* 2011 Solenoid free startup experiments in DIII-D *Nucl. Fusion* submitted